

Simulation of x-ray absorption near edge spectra of electronically excited ruthenium tris-2,2'-bipyridine

Luke Campbell

Department of Chemistry, Rowland Hall, University of California, Irvine, California 92697 and Lawrence Berkeley National Laboratory, Berkeley, California 94720

Shaul Mukamel^{a)}

Department of Chemistry, Rowland Hall, University of California, Irvine, California 92697

(Received 9 August 2004; accepted 17 September 2004)

The L_3 edge x-ray absorption near edge spectrum (XANES) of the ground electronic state and the metal to ligand charge transfer state of ruthenium tris-2,2'-bipyridine is calculated. The final valence states and energies in the presence of the photoelectron and core hole, and the corresponding transition intensities are computed using time dependent density functional theory with the Becke three-parameter density functional with the Lee-Yang-Parr correlation functional. Calculations show a valence shift of the primary XANES peak and the appearance of the new XANES transition to the hole created by the optical excitation, in agreement with experiment [M. Saes, C. Bressler, R. Abela, D. Grolimund, S. L. Johnson, P. A. Heimann, and M. Chergui, *Phys. Rev. Lett.* **90**, 047403 (2003)].

© 2004 American Institute of Physics. [DOI: 10.1063/1.1814101]

I. INTRODUCTION

X-ray absorption near edge spectroscopy (XANES) uses x-ray photons tuned to just above (0–10 eV) the absorption threshold of a target element. The absorption of such photons promotes an electron from a selected core into an unoccupied bound valence orbital. Because the transition can only occur when the final orbital has a significant amplitude near the core orbital, this technique essentially measures the unoccupied density of states in the vicinity of the absorbing atom.

The advent of picosecond to attosecond x-ray pulses has opened the door to time resolved x-ray spectroscopies.¹ In optical pump/x-ray probe measurements,² an ultrafast optical laser pulse prepares the system in a transient state, and can induce geometry changes upon electronic excitation due to photodissociation, changes in conformation, vibrations, and other relaxation processes. These are then monitored by the x-ray probe pulse. The shifts in atomic positions will affect the final state energies and the intensity of the transitions, and can thus be seen in XANES as shifts in peak positions and intensities. The change in charge distribution upon electronic excitation will also affect the final state energies. This effect can be demonstrated in a charge transfer excitation; if an electron is taken away from the absorbing atom, it will take more energy to excite the core electron to orbitals farther from the now more highly charged atom. Furthermore, when electrons are removed from orbitals, new XANES peaks can appear because of the newly opened transitions from the core to the recently vacated valence orbitals. This is illustrated in Fig. 1. Similarly, if an electron is put into a previously unoccupied orbital, a peak in the ground state XANES can disappear.

There already exist codes that can calculate the XANES

for the electronic ground state of an arbitrary atomic geometry, such as the real space multiple scattering Green's function code FEFF (Ref. 3) and the transition state density functional theory code STOBED-MON.⁴ However, simulations of time resolved optical pump, x-ray probe experiments require calculating XANES of electronic excited states. In Sec. II we present a computational algorithm which accomplishes this. Section III applies this method to the organometallic complex ruthenium tris-2,2'-bipyridine, and comparison is made with experimental spectra.⁵ Section IV discusses the importance of many-electron effects and outlines possible future work.

II. THE DEEP-CORE HAMILTONIAN

The deep-core Hamiltonian first proposed by Nozieres and The DeDominicis, and by Langreth,^{6–8} has long been used for the modeling of core hole excitations. When a core orbital g becomes unoccupied by the absorption of an x-ray photon, the valence electrons respond to the potential created by the core hole. Since only one core hole is present at any time, we can consider noninteracting core electrons. Core-valence exchange is neglected except insofar as it can be included in the core hole–valence potential. We take a form of this Hamiltonian that explicitly represents the electron-electron interactions among finite molecular valence orbitals

$$H = \sum_{lm}^{\text{val}} \epsilon_{lm} c_l^\dagger c_m + \sum_g^{\text{core}} \epsilon_g c_g^\dagger c_g + \sum_{jklm}^{\text{val}} V_{jklm} c_j^\dagger c_k^\dagger c_m c_l + \sum_g^{\text{core}} \sum_{lm}^{\text{val}} U_{lm,g} c_l^\dagger c_m c_g c_g^\dagger, \quad (1)$$

where c_i (c_i^\dagger) is the annihilation (creation) operator for an electron in orbital i . We work in atomic units where $m_e = \hbar = e = 1$.

^{a)}Electronic mail: smukamel@uci.edu

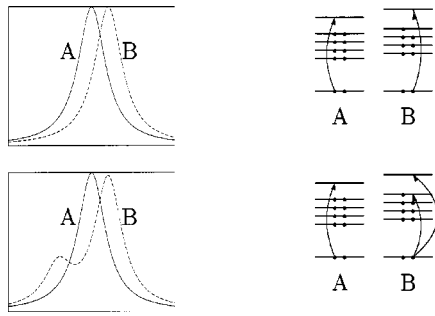


FIG. 1. Schematic of the expected effects of a charge transfer excitation. Above: When an optical excitation increases the charge of an atom, it takes more energy to excite the core electron away from the extra overall positive charge. This is diagramed on the right, where (a) represents the ground state and (b) the charge transfer state. The picture on the left illustrates the expected change to the XANES as a result of this charge transfer; the ground state (a) is shown as a solid line and the charge transfer state (b) is shown dashed and exhibits blueshifting. Below: After a charge transfer excitation, a new transition for the core hole is possible to the hole that resulted from the charge transfer. This is illustrated with the new arrow on diagram (b) on the right hand side, and by a new peak in the expected (dashed) spectrum on the left.

Valence electron-electron interactions are accounted for by the V_{jklm} potential, which is the Coulomb operator between orbitals j , k , l , and m ,

$$V_{jklm} = \int d\mathbf{x}_1 d\mathbf{x}_2 \langle j | \mathbf{x}_1 \rangle \langle k | \mathbf{x}_2 \rangle \frac{1}{|\mathbf{r}_1 - \mathbf{r}_2|} \langle \mathbf{x}_1 | l \rangle \langle \mathbf{x}_2 | m \rangle$$

and we use the variable $\mathbf{x} = (\mathbf{r}, s)$ to represent both space and spin coordinates. The one electron Hamiltonian includes the electron kinetic energy, the Coulomb attraction to the nuclei, and the Coulomb and exchange interaction with all core electrons,

$$\epsilon_{lm} = \langle l | -\frac{\hat{\mathbf{p}}^2}{2} + \sum_a^{nucl} \frac{Z_a}{|\hat{\mathbf{r}} - \mathbf{r}_a|} | m \rangle + \sum_g^{core} [V_{lmg} - V_{lggm}] c_g^\dagger c_g,$$

where nucleus a has charge Z_a and position \mathbf{r}_a , and where $\hat{\mathbf{r}}$ and $\hat{\mathbf{p}}$ are the electron position and momentum operators. The core energy ϵ_g is the energy required to remove the core electron in the absence of valence relaxation.

Strictly speaking, the core hole-valence electron interaction $U_{lm,g}$ includes both the Coulomb attraction and the exchange interaction between the electrons in valence orbitals l , m and the core hole in orbital g ; $U_{lm,g} = -V_{lmg} + V_{lggm}$. However, we will take the core hole into account in an approximate way: since it is highly localized in a volume much smaller than the typical extent of the valence electrons we will replace the core hole by a point charge at the nucleus. This is equivalent to the valence electrons being subjected to the field of a nucleus of charge $Z+1$ for the absorbing atom rather than Z . The practical consequence of this “ $Z+1$ approximation”⁹ is that we may focus solely on valence excitations in the core excited state without having to worry about calculations of the deep-core excitation. This is an additional approximation to Eq. (1), in which the core-valence potential U is taken as

$$U_{lm,g} = \langle l | \frac{1}{|\hat{\mathbf{r}} - \mathbf{r}_0|} | m \rangle,$$

where \mathbf{r}_0 is the position of the absorbing atom.

Initially the molecule is in the electronic state $|\Psi_i\rangle$ with energy E_i , which can be either the ground state or an electronic excited state. We denote the final electronic states after absorption of the x-ray photon as $|\Psi_f\rangle$ with energies E_f . Fermi's golden rule describes the absorption of the x-ray photon with frequency ω and polarization ν as

$$\sigma_{\text{abs}}(\omega, \nu) = \frac{4\pi^2}{\omega c} \sum_f |\langle \Psi_i | \mu^\nu | \Psi_f \rangle|^2 \delta(\omega + E_i - E_f). \quad (2)$$

The electronic dipole operator in the direction ν is

$$\mu^\nu = \sum_{gj} \mu_{gj}^\nu c_g c_j^\dagger, \quad (3)$$

where μ_{gj}^ν is the one electron dipole matrix element,

$$\mu_{gj}^\nu = \langle g | \vec{v} \cdot \hat{\mathbf{p}} | j \rangle, \quad (4)$$

where \vec{v} is the unit vector along ν .

In our model, any given core excited final state can be coupled to the fully core occupied initial state by the creation or annihilation operator for a single core orbital. Thus, substituting Eq. (3) in Eq. (2) gives

$$\sigma_{\text{abs}}(\omega, \nu) = \frac{4\pi^2}{\omega c} \sum_{g,lm} \sum_f \mu_{lg}^\nu \mu_{gm}^\nu \langle \Psi_i | c_l c_g^\dagger | \Psi_f \rangle \times \langle \Psi_f | c_g c_m^\dagger | \Psi_i \rangle \delta(\omega + E_i - E_f). \quad (5)$$

The deep-core Hamiltonian [Eq. (1)] gives separate eigenvalue problems for the core and valence electrons, allowing us to factorize the all-electron wave function $|\Psi\rangle$ into a product of a fully correlated N electron valence wave function $|\Phi^N\rangle$ and the ground state core wave function $|G_0\rangle$, $|\Psi_i\rangle = |\Phi^N\rangle |G_0\rangle$; or an $N+1$ electron valence wave function $|\Phi'^{N+1}\rangle$ and the core wave function when the core orbital g is unoccupied $|G'_g\rangle$, $|\Psi_f\rangle = |\Phi'^{N+1}\rangle |G'_g\rangle$. The prime implies that the valence wave function is calculated in the presence of the core potential. Using this notation, we rewrite the deep-core Hamiltonian as

$$H = |G_0\rangle H_i \langle G_0| + \sum_g |G'_g\rangle H_f^\dagger \langle G'_g|, \quad (6)$$

where we have defined the effective valence electron Hamiltonians

$$H_i = \sum_{g'} \epsilon_{g'} + \sum_{lm} \epsilon_{lm} c_l^\dagger c_m + \sum_{jklm} V_{jklm} c_j^\dagger c_k^\dagger c_m c_l, \quad (7)$$

$$H_f^\dagger = \sum_{g' \neq g} \epsilon_{g'} + \sum_{lm} [\epsilon_{lm} + U_{lm,g}] c_l^\dagger c_m + \sum_{jklm} V_{jklm} c_j^\dagger c_k^\dagger c_m c_l. \quad (8)$$

We note that $c_g |G_0\rangle = |G'_g\rangle$, $c_g^\dagger |G_0\rangle = 0$, $c_g^\dagger |G'_g\rangle = |G_0\rangle \delta_{gg}$, and that $c_g |G'_g\rangle$ takes us out of the relevant space of single core excitations.

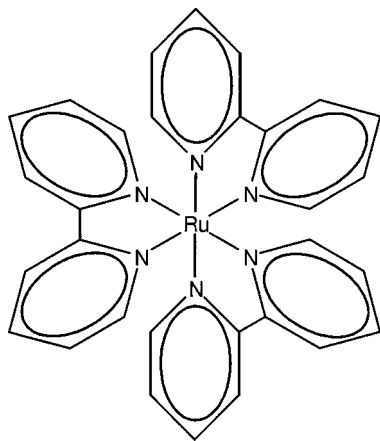


FIG. 2. The geometry of the complex $\text{Ru}(\text{bpy})_3^{2+}$. The three bipyridine ligands are mutually perpendicular, with the nitrogens octahedrally coordinated about the ruthenium.

When the wave functions in Eq. (5) are factorized into products of core and valence states, we obtain

$$\sigma_{\text{abs}}(\omega, \nu) = \frac{4\pi^2}{\omega c} \sum_f \sum_{g,lm} \mu_{lg}^\nu \mu_{gl}^\nu \langle \Phi_i^N c_l | \Phi_f'^{N+1} \rangle \times \langle \Phi_f'^{N+1} | c_m^\dagger \Phi_i^N \rangle \delta(\omega + E_i - E_f). \quad (9)$$

The orbitals in the sum are those computed self-consistently for the filled core state. We write $c_l^\dagger |\Phi_i^N\rangle = |c_l^\dagger \Phi_i^N\rangle$ to emphasize that this is a nonstationary state of H_f^g and that $\langle \Phi_f'^{N+1} | c_l^\dagger \Phi_i^N \rangle$ is a many-body overlap in the $N+1$ electron space. To account for the core-hole lifetime broadening, we add a finite linewidth Γ which can be read from tabulated values for any given core orbital g . In addition, for an isotropic sample, we will need to average over all x-ray polarizations. This finally leads to

$$\sigma_{\text{abs}}(\omega) = \frac{4\pi}{3\omega c} \sum_f \sum_{g,lm} \sum_\nu \mu_{lg}^\nu \mu_{gm}^\nu \times \frac{\langle \Phi_i^N c_l | \Phi_f'^{N+1} \rangle \langle \Phi_f'^{N+1} | c_m^\dagger \Phi_i^N \rangle \Gamma}{(\omega + E_i - E_f)^2 + \Gamma^2}. \quad (10)$$

Calculating the x-ray absorption thus requires three ingredients whose calculations are detailed in the appendixes: the dipole matrix elements μ_{lg}^ν (Appendix A), overlaps between the many-electron states $|c_l^\dagger \Phi_i^N\rangle$ and $|\Phi_f'^{N+1}\rangle$ (Appendix B), and the resonant transition energies $E_i - E_f$ (Appendix C). In the following section we apply this procedure to the XANES of a metal to ligand charge transfer (MLCT) state of an organometallic complex.

III. APPLICATION TO RUTHENIUM TRIS-2,2' BIPYRIDINE

We now focus our attention on the L_3 edge XANES of ruthenium tris-2,2'-bipyridine [$\text{Ru}(\text{bpy})_3^{2+}$] (Fig. 2). The photophysics of this organometallic complex has been well studied.^{10,11} Upon optical excitation to a Franck-Condon state, a rapid cascade of decays occurs to a singlet MLCT state, which undergoes intersystem crossing to a triplet MLCT state. These initial reactions are complete within

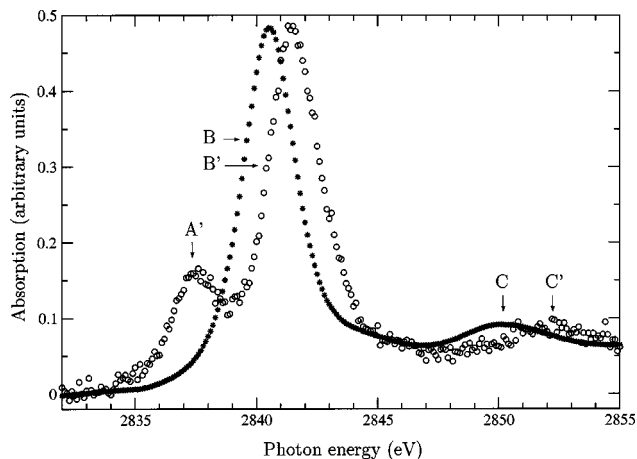


FIG. 3. The experimental XANES of $\text{Ru}(\text{bpy})_3^{2+}$ (Ref. 5). The spectrum originating from the MLCT (ground) state is shown as circles (stars). Peaks B and C appear in the ground state spectrum. In the MLCT state, these peaks are blueshifted by a valence shift to B' and C' , while a new peak A' appears due to the new transition to the optically created hole.

300 fs.¹² The triplet MLCT state, however, is long lived with a lifetime of microseconds. Recent experimental XANES measurements of the ground and triplet MLCT are displayed in Fig. 3.⁵ They show a valence shift of peak B to B' and the appearance of a new XANES peak corresponding to the optical hole, labeled as peak A' . Our goal is to simulate these spectra at the *ab initio* level.

A singlet ground state calculation of $\text{Ru}(\text{bpy})_3^{2+}$ using the 3-21G basis set was carried out with the Becke three-parameter density functional¹³ and the Lee-Yang-Parr correlation functional¹⁴ with the GAUSSIAN 03 code. The $\text{Ru}(\text{bpy})_3^{2+}$ geometry was taken from x-ray crystallography.¹⁵⁻¹⁷ The first 15 singlet and 5 triplet excited states were calculated with time dependent density functional theory (TDDFT). To describe the lowest energy core state we use the same basis set and density functionals as for the ground state, but include the core hole via the $Z+1$ approximation with a calculation on the doublet spin $\text{Ru}(\text{bpy})_3^{2+}$. The first 50 excitations were calculated with TDDFT. Table I lists the overlaps between orbitals in the ground state $|\Phi_0^N\rangle$ and the lowest core excited state $|\Phi_0'^{N+1}\rangle$ that are important for our analysis, chosen as the valence orbitals present in the calculated excited states that had the greatest dipole coupling to the excited core orbitals. Orbital 144 from $|\Phi_0^N\rangle$ and 141 from $|\Phi_0'^{N+1}\rangle$ are clearly identifiable as the $d_{3z^2-r^2}$ ruthenium atomic orbital. Orbitals 142, 143, 157, and 158 from $|\Phi_0^N\rangle$ are also primarily of ruthenium d character, as are orbitals 139, 140, 148, and 149 of $|\Phi_0'^{N+1}\rangle$, although these are mixtures of the pure angular momentum d eigenstates. All other listed orbitals are localized primarily on the ligands. The core excitation energies were computed using the single configuration Dirac-Fock code SCF DAT (Ref. 18) to pin down the absorption edge, as described in Appendix C.

The calculation of XANES from an optically excited state involves two particle-hole excitations, one for the initial optical transition and one for the x-ray transition. Our factorization of the full wave function into a valence and core

TABLE I. The overlap matrix between selected orbitals of the ground state (G.S.) wave function (with 144 alpha spin electrons) and the $Z+1$ wave function (with 145 alpha spin electrons). The table is split into “occupied” (orbitals 139–145) and “unoccupied” (orbital numbers >145) blocks, using the conventions given in the main text. The small elements in the off-diagonal blocks allow us to use single excitations of the ground state $Z+1$ wave function to represent the excited states important to XANES. The orbitals listed here are either states with significant Ru d character, and thus with a large dipole coupling to the $2p$ core orbitals, or are the ligand centered orbitals occupied in the MLCT excitations, in addition to being the highest occupied and lowest unoccupied orbitals (these are the orbitals for which occupied-unoccupied block mixing is of most concern, as deeper orbitals tend to mix among themselves, as do higher virtual orbitals). Orbital 144 from the ground state and 141 from the $Z+1$ state are clearly identifiable as the $d_{3z^2-r^2}$ ruthenium atomic orbital. Ground state orbitals 142, 143, 157, and 158 are also primarily of ruthenium d character, as are orbitals 139, 140, 148, and 149 of the $Z+1$ state, although these are mixtures of the pure angular momentum d eigenstates. All other listed orbitals are primarily located on the ligands.

Z+1\G.S.	139	140	141	142	143	144	145	146	147	157	158
139	0.02	-0.13	0.10	0.77	0.39	-0.13	0.01	-0.11	-0.01	0.00	0.00
140	0.08	0.18	-0.13	0.38	-0.79	-0.10	0.00	0.01	-0.12	0.00	-0.00
141	-0.37	0.01	-0.09	0.18	-0.04	0.82	0.01	-0.02	-0.02	0.00	0.00
142	-0.57	0.74	0.24	0.10	-0.08	-0.24	0.00	0.00	-0.01	0.00	0.00
143	0.69	0.65	0.14	0.11	0.04	0.24	0.00	-0.01	0.00	0.00	0.00
144	0.22	-0.09	0.94	-0.03	-0.15	0.18	0.00	0.01	-0.01	0.00	0.00
145	0.00	0.00	0.00	0.00	0.00	0.01	0.99	-0.06	-0.05	-0.03	-0.03
146	0.00	0.01	-0.01	-0.10	-0.10	-0.01	-0.04	-0.95	0.24	0.02	-0.01
147	0.00	0.01	0.01	-0.10	0.10	0.00	-0.06	-0.24	-0.95	0.00	0.00
148	0.00	0.00	0.00	0.00	0.00	0.00	0.04	0.01	0.00	0.93	0.05
149	0.00	0.00	0.00	0.01	0.00	0.01	0.02	-0.01	0.00	-0.08	0.94

wave function replaces the core excitation with the problem of finding the excitations of the additional electron put into the final valence state $|\Phi_f^{N+1}\rangle$. As a result, for XANES calculations of an arbitrary initial excited state, we need to include doubly excited Slater determinants (two electron-hole pairs) as illustrated in Fig. 4. TDDFT excited states involve only single excitations. However, there are initial states for which only single excitations of the lowest core excited state $|\Phi_0^{N+1}\rangle$ are necessary to describe the XANES. This can be illustrated by considering a system where the orbitals hardly change between the core occupied and unoccupied states. The state $|\Phi_0^{N+1}\rangle$ has a highest occupied molecular orbital (HOMO) denoted l_{\max} , all orbitals with lower energy are occupied. Consider an initial state wave function $|\Phi_i^N\rangle$ for which no orbital with higher energy than l_{\max} is occupied, and which has one hole in orbital l such that $\epsilon_l < \epsilon_{l_{\max}}$. The excitations of the electron in orbital l of

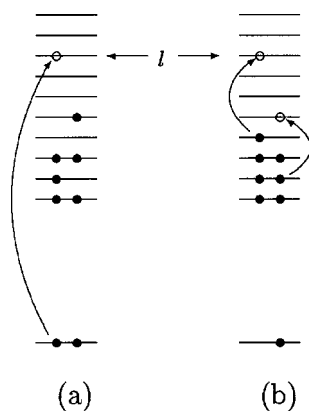


FIG. 4. Diagram (a) represents a molecule with a single particle-hole type excitation among its N valence electrons. The x-ray induced transition from the core to orbital l is shown. Diagram (b) shows the ground valence state of the core excited molecule, with $N+1$ valence electrons. The two excitations of (b) necessary to achieve significant overlap between (b) and (a) are shown as arrows, occupied orbitals are designated by solid circles, and the orbitals about to be occupied by the transitions are shown with open circles.

$|\Phi_0^{N+1}\rangle$ are those which will have significant overlap with $|c_m^\dagger \Phi_i^N\rangle$, and thus for this state, only single excitations need be considered. The true initial ground state $|\Phi_0^N\rangle$ is one such state, as are excitations of $|\Phi_0^N\rangle$ from any occupied orbital to orbital l_{\max} . This is illustrated in Fig. 5.

For more general electronic excitations, there will be blocks of orbitals in the overlap matrix T_{lm} between orbitals l in $|\Phi_0^{N+1}\rangle$ and m in $|\Phi_0^N\rangle$ which are not approximately diagonal. For such systems, only single excitations are necessary to describe the XANES as long as all the large elements of T are confined to the “occupied-occupied” ($l, m \leq l_{\max}$) and “unoccupied-unoccupied” ($l, m > l_{\max}$) blocks of

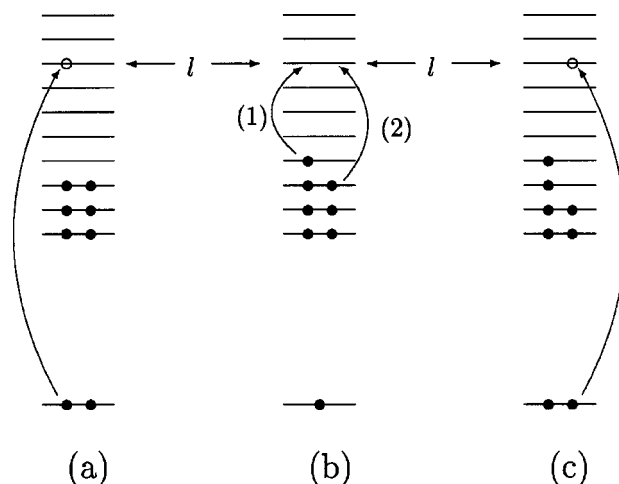


FIG. 5. Diagram (a) illustrates the x-ray induced transition of a core electron to orbital l for the ground state of a molecule with N valence electrons. The single excitation (labeled 1) of the ground $N+1$ valence electron state of the core excited molecule to orbital l [shown in diagram (b)] will give significant overlap with the state illustrated in (a). A single excitation of the state (b) can also give significant overlap with a certain set of valence excited states, an example of which is shown in diagram (c) and which is reached by the excitation labeled 2. The excitations are shown as arrows, occupied orbitals are designated by dots, and the orbitals about to be occupied by the transitions are shown with circles.

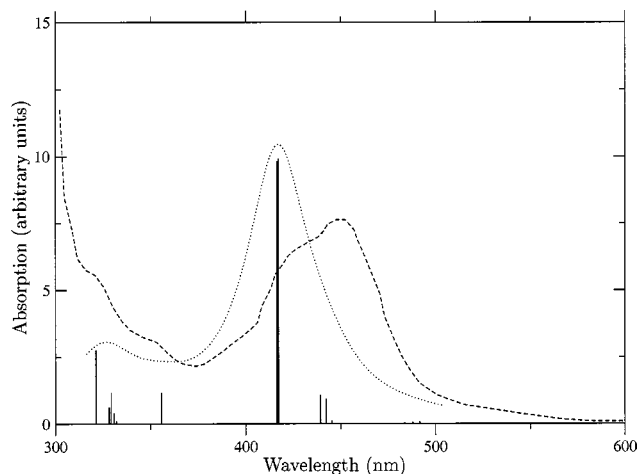


FIG. 6. Stick spectrum: the calculated optical transitions of $\text{Ru}(\text{bpy})_3^{2+}$. Dots: calculated optical spectrum broadened by a Lorentzian linewidth with a full width at half maximum of 40 nm. Dashes: the experimental optical absorption spectrum (Ref. 12).

the matrix. (Note that the term occupied-occupied is a bit of a misnomer, since $|\Phi_i^N\rangle$ will have at least one unoccupied orbital in this block.) Further, $|\Phi_i^N\rangle$ must have one and only one unoccupied orbital within the occupied-occupied block and no occupied orbitals in the unoccupied-unoccupied block.

Table I shows the important segments of the orbital overlap matrix. The elements of the “occupied-unoccupied” and “unoccupied-occupied” blocks are small. The lowest three TDDFT calculated excited states of core filled $\text{Ru}(\text{bpy})_3^{2+}$ are nearly degenerate triplet MLCT states depopulating the $4d_{z-r}$ orbital. The third of these is almost entirely composed of a transition from the HOMO to LUMO (lowest unoccupied molecular orbital) of the ground state, with amplitude 0.95. The TDDFT final state excitations can thus describe the XANES from this initial state. Because x-ray absorption is local to the absorbing atom, and the differences between the three triplet MLCT states occur well out on the ligands, we expect the XANES from all three to be similar, and use the calculation of the one state as representative of all three. Since orbital 144 in $|\Phi_0^N\rangle$ most closely corresponds to orbital 141 in $|\Phi_0^{N+1}\rangle$ excited states $|\Phi_f^{N+1}\rangle$ resulting from single excitations from orbital 141 in $|\Phi_0^{N+1}\rangle$ will be the dominant contribution to the XANES from this excited state.

TDDFT represents the excited state as a single Slater determinant with a different set of orbitals than the ground state. The excited states can alternatively be expanded as a linear combination of the excited Slater determinants of ground state orbitals. This configuration interaction (CI) representation is convenient for the present simulation, since the orbital overlaps need only be described for the ground valence state $|\Phi_0^N\rangle$ and the lowest core excited valence state $|\Phi_0^{N+1}\rangle$ (as will be done below), and need not be repeated for every excited state $|\Phi_f^{N+1}\rangle$.

The TDDFT calculation for the core filled $\text{Ru}(\text{bpy})_3^{2+}$ gave two strongly optically active transitions at 2.9776 eV (416.38 nm) and 2.9829 eV (415.65 nm) of nearly equal intensity ($f=0.0990$ and 0.0980, respectively) for

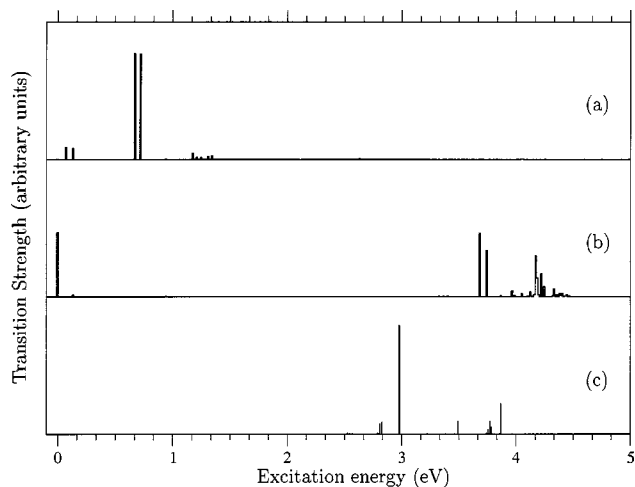


FIG. 7. The energies of the excited states involved in the L_3 x-ray transitions from the ground state (a) and MLCT state (b) of $\text{Ru}(\text{bpy})_3^{2+}$ and in the optical transitions (c). The energies of the states are plotted on the x axis zeroed at the valence ground state energy, with a height given by the intensity of the transition. This demonstrates that XANES and optical measurements access different excited states.

$\text{Ru}(\text{bpy})_3^{2+}$ in vacuo. The experimental optical absorption spectrum¹² shows two strong transitions at 425 nm and 460 nm of similar intensity for $[\text{Ru}(\text{bpy})_3](\text{PF}_6)_2$ in CH_3CN solution. The calculated and experimental spectra are compared in Fig. 6. The agreement is reasonable given the difference in solvents. Our calculated XANES spectrum is dominated by transitions of the ruthenium $2p$ core orbitals to a ruthenium $4d$ orbital. The optical spectrum, on the other hand, is dominated by transitions from the two lowest lying $4d$ orbitals (orbitals 142 and 143 from $|\Phi_0^N\rangle$) to the three lowest unoccupied orbitals (145, 146, and 147 from $|\Phi_0^N\rangle$) located on the ligands. [Note that after electronic relaxation to the long lived triplet MLCT state, the hole is in the $4d_{3z^2-r^2}$ orbital 144 of $|\Phi_0^N\rangle$ and the electron in 145, 146, or 147 of $|\Phi_0^N\rangle$.] X rays thus access significantly different orbitals compared to visible light. Figure 7 shows the final excited state energies of the x ray and optical transitions weighted by their transition strengths. This again demonstrates that the x rays reveal a different part of the manifold of electronic excitations than visible light.

When an electron from a doubly occupied core orbital is excited to the valence levels, it is equally likely to be spin up or spin down with respect to any spin orientation of the original valence state. Ideally, for single excitation methods,

TABLE II. Matrix of the product of dipole matrix elements $\sum_{g\nu} \mu_{lg}^\nu \mu_{gm}^\nu$ summed over the $2p$ cores g and x-ray polarizations ν for the six orbitals with the strongest dipole coupling to the $2p$ core orbitals.

Ωm	144	146	147	157	158	162
144	1.68	-0.02	0.01	0.00	0.01	0.00
146	-0.02	0.15	0.00	-0.02	0.01	0.00
147	0.01	0.00	0.17	0.01	0.01	0.00
157	0.00	-0.02	0.01	1.63	0.01	-0.40
158	0.01	0.01	0.01	0.01	1.60	0.10
162	0.00	0.00	0.00	-0.40	0.10	0.10

TABLE III. Matrix of overlap factors $\langle \Phi_{i c_l} | \Phi_f' \rangle \langle \Phi_f' | c_m^\dagger \Phi_i \rangle$ for the two excited final states that give the largest contribution to the ground state XANES spectrum. The transition strength to a given final excited state is proportional to the trace of the product of the matrix given in Table II and the overlap matrix for the final state.

Excited state 3						Excited state 4					
$l \setminus m$	146	147	157	158	162	$l \setminus m$	146	147	157	158	162
146	0.00	0.00	0.01	0.00	0.00	146	0.00	0.00	0.00	-0.01	0.00
147	0.00	0.00	0.01	0.00	0.00	147	0.00	0.00	0.00	0.00	0.00
157	0.01	0.00	0.69	0.05	-0.12	157	0.00	0.00	0.00	-0.04	0.00
158	0.00	0.00	0.05	0.00	-0.01	158	-0.01	0.00	-0.04	0.68	0.04
162	0.00	0.00	-0.12	-0.01	0.02	162	0.00	0.00	0.00	0.04	0.00

the sum over all excited states $|\Phi_f'^{N+1}\rangle$ used to represent this photoelectron would thus include spin flip excitations from the ground state core excited valence wave function $|\Phi_0'^{N+1}\rangle$. Standard methods for calculating excited states however, such as TDDFT or CIS, maintain the electron spin. As such, for initial valence states with a definite spin orientation we only calculated the excited state configurations with one particular photoelectron spin (this should be obvious by examining Fig. 5 and trying to represent both spin occupations of orbital l in the right hand configuration with a single excitation from the center configuration).

To work with single excitations that do not include spin flips, we made the approximation that the energy is invariant to spin flips of the photoelectron. Thus (assuming a singlet ground state), for any given spatial core orbital there are two core excitations to initial state orbitals l which do not have the optical hole or the optically excited electron, but only one such excitation when l contains the optical hole or optically excited electron. As such, the transition intensity is multiplied by 2 to account for both possible spin states when the transition is to an initial state orbital not involved in the optical transition.

As expected, the dipole coupling from the ruthenium $2p$ core orbitals to the orbitals with strong ruthenium $4d$ character is the strongest of any coupling to the $2p$ orbitals. The

matrix of dipole coupling factors for the most important orbitals is given in Table II. The average dipole coupling to the $4d$ orbitals 144, 157, and 158 in $|\Phi_0^N\rangle$ is dominant. The $4d$ orbitals 142 and 143 in $|\Phi_0^N\rangle$ are not shown since they are always occupied, and thus do not participate in the x-ray transitions.

The overlap matrices of the dominant excitations are shown in Table III for the ground state and in Table IV for the MLCT state. Figure 8 depicts the transition intensities plotted against the x-ray energy of the transition while Tables V and VI list the intensities. It is clear from Fig. 8 and Table V that the ground state XANES is dominated by two closely spaced transitions, corresponding to the third and fourth excited states of $|\Phi_0'^{N+1}\rangle$. In these states the wave function is almost entirely described by the excitation of ligand located orbital 145 of $|\Phi_0'^{N+1}\rangle$ to one of the unoccupied $4d$ orbitals (either 148 or 149 of $|\Phi_0'^{N+1}\rangle$, corresponding to orbitals 157 and 158 of $|\Phi_0^N\rangle$). No other significant XANES transitions occur in the 50 excited states calculated. The situation for the MLCT state is more complex. There is a strong transition where the photoelectron occupies the $4d_{3z^2-r^2}$ optical hole, corresponding to the ground state of $|\Phi_0'^{N+1}\rangle$. The peaks corresponding to the photoelectron occupying the higher $4d$

TABLE IV. Matrix of overlap factors $\langle \Phi_{i c_l} | \Phi_f' \rangle \langle \Phi_f' | c_m^\dagger \Phi_i \rangle$ for the four excited final states that give the largest contribution to the MLCT state XANES spectrum. The transition strength to a given final excited state is proportional to the trace of the product of the matrix given in Table II and the overlap matrix for the final state.

Ground state							Excited state 18						
$l \setminus m$	144	146	147	157	158	162	$l \setminus m$	144	146	147	157	158	162
144	0.71	0.00	0.00	0.00	0.00	0.00	144	0.00	0.00	0.00	0.00	0.00	0.00
146	0.00	0.00	0.00	0.00	0.00	0.00	146	0.00	0.00	0.00	0.00	0.00	0.00
147	0.00	0.00	0.00	0.00	0.00	0.00	147	0.00	0.00	0.00	0.00	0.00	0.00
157	0.00	0.00	0.00	0.00	0.00	0.00	157	0.00	0.00	0.00	0.21	0.02	-0.03
158	0.00	0.00	0.00	0.00	0.00	0.00	158	0.00	0.00	0.00	0.02	0.00	0.00
162	0.00	0.00	0.00	0.00	0.00	0.00	162	0.00	0.00	0.00	-0.03	0.00	0.01
Excited state 19							Excited state 31						
$l \setminus m$	144	146	147	157	158	162	$l \setminus m$	144	146	147	157	158	162
144	0.00	0.00	0.00	0.00	0.00	0.00	144	0.00	0.00	0.00	0.00	0.00	0.00
146	0.00	0.00	0.00	0.00	0.00	0.00	146	0.00	0.00	0.00	0.02	0.00	0.00
147	0.00	0.00	0.00	0.00	0.00	0.00	147	0.00	0.00	0.00	0.02	0.00	0.00
157	0.00	0.00	0.00	0.00	-0.01	0.00	157	0.00	0.02	0.02	0.13	-0.01	-0.02
158	0.00	0.00	0.00	-0.01	0.15	0.01	158	0.00	0.00	0.00	-0.01	0.00	0.00
162	0.00	0.00	0.00	0.00	0.01	0.00	162	0.00	0.00	0.00	-0.02	0.00	0.00

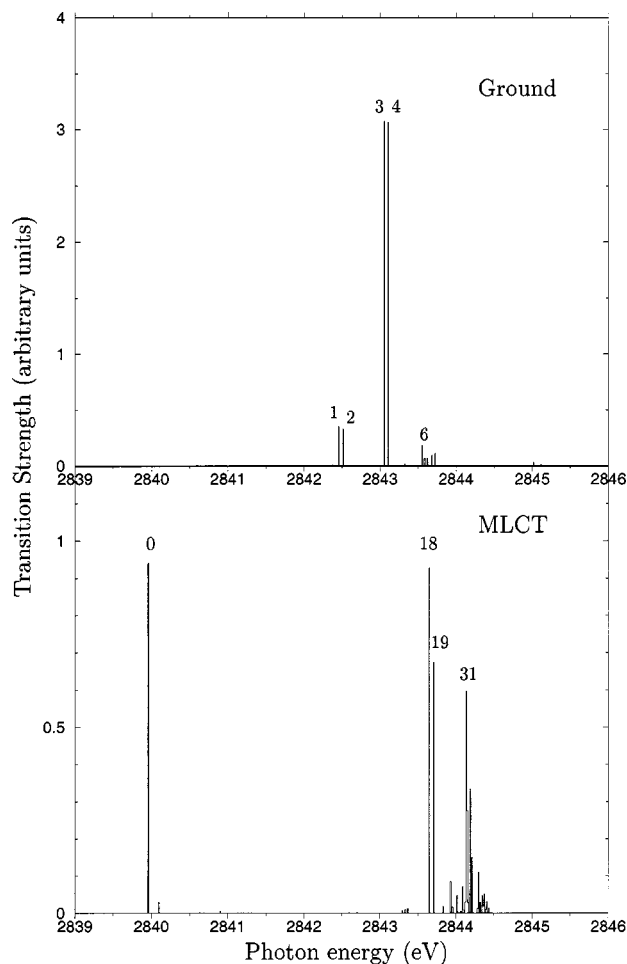


FIG. 8. Transitions participating in the L_3 edge XANES labeled according to their excited states. Upper panel: the ground state XANES transitions. Lower panel: MLCT state XANES transitions.

orbitals are made up of many low amplitude excitations, only a few of which have overlap factors greater than 0.1. The contributions from the six orbitals listed in the dipole and overlap matrices of Tables II, III, and IV make up about 70% of the intensity of the ground state XANES transitions to excited states 3 and 4. The remainder comes from the low

TABLE V. Excited states participating in the ground state XANES. The transition intensity is listed when all orbitals are included (third column) or when only the six orbitals of Tables II and III are considered (fourth column).

State	Energy	Intensity all orbitals	Intensity selected orbitals
1	2842.447	0.35	0.25
2	2842.512	0.32	0.23
3	2843.047	3.07	2.43
4	2843.107	3.06	2.20
5	2843.322	0.01	0.01
6	2843.553	0.18	0.03
7	2843.595	0.06	0.03
8	2843.633	0.06	0.02
9	2843.689	0.09	0.00
10	2843.730	0.11	0.00
11	2845.006	0.03	0.00

TABLE VI. Excited states participating in the MLCT state XANES. The transition intensity is listed when all orbitals are included (third column) or when only the six orbitals of Tables II and IV are considered (fourth column).

State	Energy	Intensity all orbitals	Intensity selected orbitals
0	2839.965	0.94	1.19
2	2840.030	0.03	0.04
15	2843.324	0.01	0.01
16	2843.367	0.01	0.01
18	2843.647	0.93	0.74
19	2843.711	0.67	0.48
20	2843.833	0.02	0.01
21	2843.934	0.08	0.06
22	2843.958	0.02	0.01
25	2844.019	0.05	0.03
28	2844.092	0.07	0.05
29	2844.105	0.01	0.01
30	2844.126	0.03	0.03
31	2844.133	0.60	0.48
32	2844.149	0.22	0.17
33	2844.151	0.05	0.03
34	2844.159	0.03	0.02
35	2844.190	0.10	0.08
36	2844.192	0.24	0.17
37	2844.209	0.15	0.11
38	2844.279	0.01	0.01
39	2844.292	0.04	0.03
40	2844.300	0.07	0.05
42	2844.324	0.03	0.02
43	2844.340	0.05	0.03
44	2844.362	0.02	0.01
45	2844.370	0.01	0.01
46	2844.374	0.04	0.03
47	2844.393	0.01	0.01
48	2844.401	0.01	0.01
49	2844.410	0.01	0.01
50	2844.428	0.01	0.01

amplitude contributions from the other 261 unoccupied orbitals. Likewise, the amplitude for all the transitions to the states between 2831 and 2833 eV in the MLCT state XANES has about 80% of its intensity from the orbitals listed in the tables, with the remaining intensity coming from the other unlisted orbitals. Interference of these other orbitals lowers the peak intensity from the transition to the optical hole in the MLCT XANES by about 20%.

The raw simulations are shown in Fig. 9. Peak *B* for the ground state XANES is nearly a factor of 2 stronger than peak *B'* from the MLCT XANES, which differs from experiment where the *B* and *B'* peaks are equally strong. Our simulations, redshifted by 2.5 eV to correct for the L_3 edge energy, are compared with experiment in Fig. 10. The primary features of the measured XANES shown in Fig. 3 are the 1 eV “valence shift” of peak *B* to *B'* between the excited and ground state XANES, and the 4 eV splitting between peaks *A'* and *B'* in the excited state⁵ (peaks *C* and *C'* are too high of an energy and lie outside the 50 calculated excited states). The peak splittings, valence shift, and relative amplitudes of the *A'* and *B'* peaks are all in excellent agreement with the experiment.

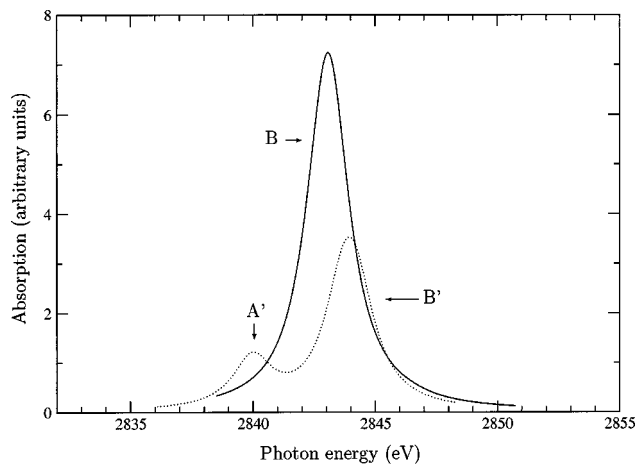


FIG. 9. The simulated L_3 edge XANES of $\text{Ru}(\text{bpy})_3^{2+}$. Solid line: ground state XANES. Dotted line: MLCT state XANES.

IV. DISCUSSION

To examine the role of the many-body overlap factors, let us consider a system of noninteracting valence electrons. The x-ray transition is then from the core orbital g to a given

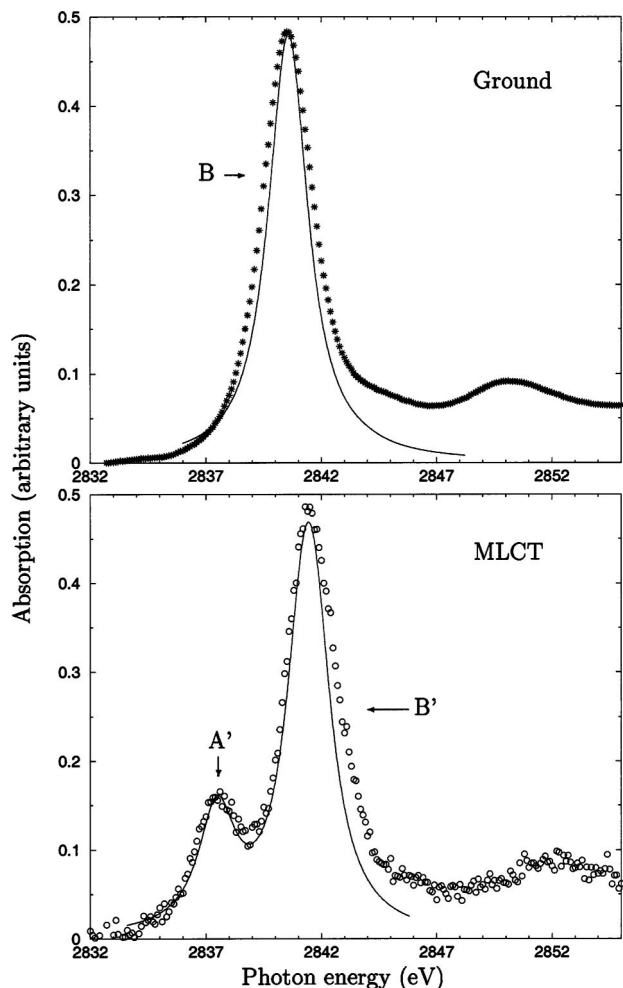


FIG. 10. The simulated L_3 edge XANES of $\text{Ru}(\text{bpy})_3^{2+}$ (lines), compared with experiment (points). The simulation spectra are scaled and redshifted by 2.5 eV. Upper panel: ground state XANES. Lower panel: MLCT state XANES.

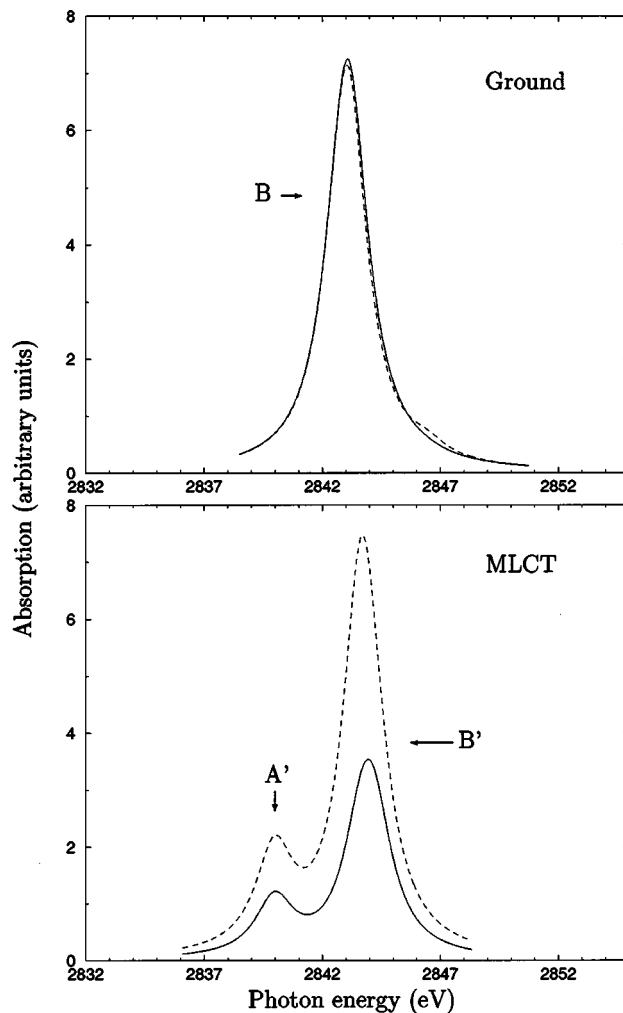


FIG. 11. Dashed lines: only the orbitals listed in Tables II, III, and IV are used to compute the L_3 edge XANES of $\text{Ru}(\text{bpy})_3^{2+}$ and we assume that only a single overlap factor with unit weight is present for any given orbital. Solid lines: the calculation using all orbitals and the full many-body overlap factors. The ground state XANES is nearly identical in both cases (upper panel). The MLCT state XANES of the full calculation is smaller by a factor of close to 2 than the approximate calculation (lower panel); in this case the approximate calculation is in better agreement with experiment, where the primary peak is nearly unchanged in amplitude in both ground and MLCT state XANES. The approximate MLCT state XANES calculation shows a slight redshift of the main peak compared to the full calculation.

valence orbital l of the lowest core excited state. For each orbital, there will be a single excited state for which the overlap factor $\langle \Phi_i^N c_l | \Phi_f'^{N+1} \rangle$ will be unity, all other excited states will give zero for that orbital. When electron-electron interactions are turned on, the energies of the valence orbitals l are modified, leading to a shift in peak position. The importance of many-electron effects can thus be seen by making certain simplifying approximations for the overlap factors $\langle \Phi_i^N c_l | \Phi_f'^{N+1} \rangle \langle \Phi_f'^{N+1} | c_m^\dagger \Phi_i^N \rangle$. We assume that for each orbital l there is a unique final state $|\Phi_f'^{N+1}\rangle$ for which $\langle \Phi_i^N c_l | \Phi_f'^{N+1} \rangle = 1$, and the contribution from all other states is zero. We take this state to be the one for which the calculated $\langle \Phi_i^N c_l | \Phi_f'^{N+1} \rangle$ is the maximum. The result of this approximation is shown in Fig. 11 when only the six orbitals listed in Tables II, III, and IV are included in the sum, and compared to the full calculation. We see that peak B' is also

redshifted compared to the full calculation. This is because two orbitals (157 and 158 of $|\Phi_0^N\rangle$) are primarily responsible for this peak, and thus only two excitations $|\Phi_f^{N+1}\rangle$ are selected when the overlaps are neglected while, as discussed earlier, this peak results from many low amplitude excitations. The two final states with the maximum overlap happen to be among the lowest energy of these, thus shifting peak B' to the red. The relative amplitudes of the ground to the MLCT state are in closer agreement to experiment than the full calculation.

When the same calculation is repeated using all orbitals, the small dipole factors from many orbitals add up to a large intensity, as shown in Fig. 12. We can interpret this as the overlaps acting to filter out the contribution from the many “spectator” orbitals, allowing us to concentrate on the orbitals primarily responsible for the signal.

Electronic excited states typically have a different geometry than the ground state. Short x-ray pulses can follow the time resolved geometry changes of a molecule after electronic excitation. To simulate such measurements, one would start in the ground state geometry but with the excited state electronic structure. A molecular dynamics simulation should then be performed to follow the trajectories of the atoms with time, and the XANES should be computed from these different configurations.

The procedure developed here is useful for the transitions to and from the lowest lying electronic valence excited states, which can be calculated accurately with quantum chemistry codes. At present, only a select class of initial electronic states can be calculated, but arbitrary low lying excited states could be described once double or higher particle-hole excitations are included. Since only the lowest energy transitions are available with this procedure, it complements rather than replaces existing extended x-ray absorption fine structure (EXAFS) calculation methods, such as the FEFF code which has proven itself in the high energy x-ray absorption regime but lacks chemical accuracy in the near edge region.

To extend the present simulation to arbitrary excited states, we will need to go beyond single excitations. This can be done by the configuration active state approach which also reduces the number of calculations needed over full doubly excited methods. In this approach, all possible excited configurations are calculated within a restricted set of orbitals. Typically, several of the highest occupied and lowest unoccupied orbitals are selected to account for correlation effects. However, using this machinery, it should be possible to include several orbitals suspected of being important in a given x-ray transition. Excited states thus only need to be calculated within this “active space.”

The limiting factor in our calculations is the computation of the excited states. It may thus be desirable to avoid such calculations altogether. By recasting Fermi’s golden rule as the imaginary part of the Fourier transform of a time-time correlation function of dipole operators we can perform a perturbation expansion on the core-hole–valence potential $U = \sum_{lm} U_{lm,g} c_l^\dagger c_m^\dagger$ using the time evolution operator in the interaction picture $S(t) = \exp_+[-if_0^t U(\tau) d\tau]$, where \exp_+ indicates a time ordered exponential. This gives

$$\begin{aligned} \sigma_{\text{abs}}(\omega, \nu) &= \frac{4\pi^2}{\omega c} \text{Im} \sum_f \int dt e^{i\omega t} e^{iE_f t} \langle \Psi_i | \mu | \Psi_f \rangle \\ &\quad \times e^{-jE_f t} \langle \Psi_f | \mu^\dagger | \Psi_i \rangle \\ &= \frac{4\pi^2}{\omega c} \text{Im} \sum_f \int dt e^{i\omega t} \langle \Psi_i | e^{iHt} \mu e^{-iHt} | \Psi_f \rangle \\ &\quad \times \langle \Psi_f | \mu^\dagger | \Psi_i \rangle \\ &= \frac{4\pi^2}{\omega c} \text{Im} \int dt e^{i\omega t} \langle \Psi_i | \mu(t) \mu^\dagger(0) | \Psi_i \rangle \\ &= \frac{4\pi^2}{\omega c} \text{Im} \sum_{lm} \mu_{lg} \mu_{gm} \int dt \\ &\quad \times e^{i(\omega - \epsilon_g)t} \langle \Phi_i | e^{iH_g t} c_l e^{-iH_g t} S(t) c_m^\dagger | \Phi_i \rangle. \end{aligned}$$

In our model, the core hole is static and structureless and does not affect the dynamics of the valence electrons except through its potential.⁶ This is equivalent to the scattering from the potential of an impurity, which is an exactly solvable model for noninteracting systems. This procedure is discussed, for example, in Mahan⁸ for infinite systems by the summation of ladder diagrams. For finite systems, a new set of eigenstates could be found by diagonalizing the valence Hamiltonian with the core-hole potential H_e . The Fourier transform of the Green’s function $\langle \Phi_i | c_l(t) c_m^\dagger | \Phi_i \rangle$ gives

$$\begin{aligned} &\int dt e^{i(\omega)t} \langle \Phi_i | c_l(t) c_m^\dagger(0) | \Phi_i \rangle \\ &= \langle \Phi_i | c_l \frac{1}{\omega - (H_e - E_i^v) - i\gamma} c_m^\dagger | \Phi_i \rangle \end{aligned} \quad (11)$$

for $H_g |\Phi_i\rangle = E_i^v |\Phi_i\rangle$. By choosing the set of orbitals of c_l and c_m^\dagger for which H_e is diagonal, the one electron Green’s function in frequency space and hence the x-ray spectrum immediately follows without the need for laborious calculations of excited states. For interacting systems, the noninteracting case could be solved at, for example, the Hartree-Fock level, and this could be used as the beginning of a perturbative calculation for the one-electron Green’s function using, for example, Hedin’s GW method which approximates the Green function as a product of a bare Green function G and a polarization W .¹⁹

Higher order optical processes can be expressed in a similar fashion but as higher order correlation functions of the dipole operator.²⁰ When one of the interactions is with an x-ray photon, an extension of this method could be applied to these nonlinear spectroscopies. In this way, x-ray pump, optical probe experiments could be simulated.

In this work we have used a quantum chemistry code which represents the electronic structure as an expansion in Gaussian basis functions in real space. This works quite well for chemical energies (up to about 10 eV) but at higher energies the limited basis set is inadequate for the necessary photoelectron states. A plane wave basis set has the possibility of enabling the calculation of parts of the extended x-ray absorption spectrum for excited states, including the EXAFS, which is useful for structure determination.

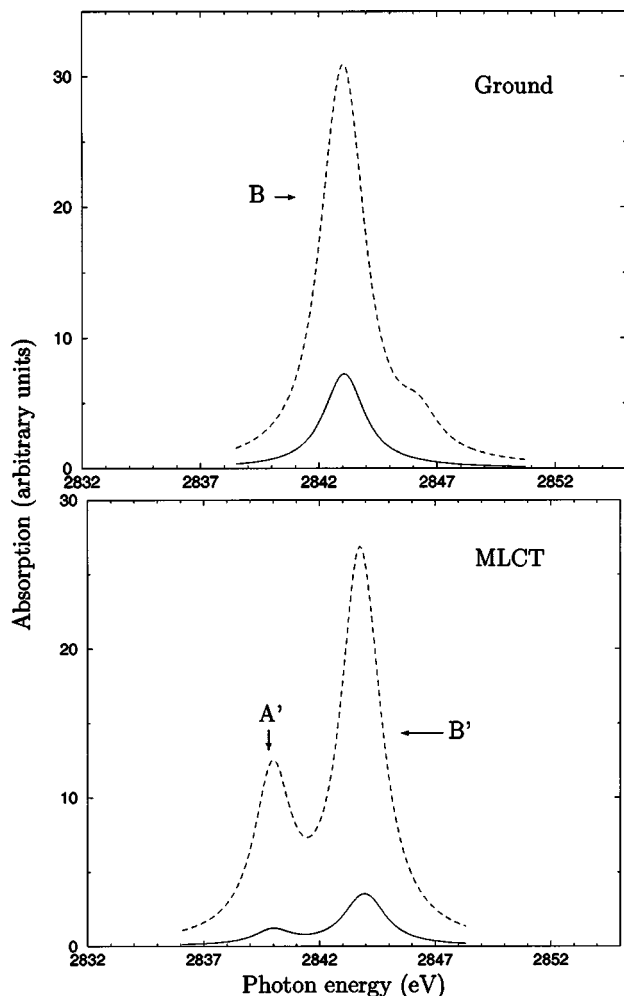


FIG. 12. When we assume that only a single overlap factor with unit weight is present for any given orbital in our simulations but we include all orbitals (dashed lines), the results have significantly increased amplitude compared to the calculation with full overlaps (solid lines). The overlaps thus serve to filter out the contributions from all the spectator orbitals.

ACKNOWLEDGMENTS

The authors would like to thank Dr. Robert Schoenlein for many stimulating discussions. They also thank Christian Bressler, Melanie Saes, Wojciech Gawelda, and Majed Cherbul for helpful discussions as well as for sharing their results. This work was supported by the Laboratory Directed Research and Development Program of Lawrence Berkeley National Laboratory under the Department of Energy Contract No. DE-AC03-76SF00098. The support of DOE Grant No. DE-FG02-04ER15571 is gratefully acknowledged.

APPENDIX A: THE DIPOLE MATRIX ELEMENTS

We expand the molecular orbitals in Gaussian basis functions²¹

$$\phi_d(\mathbf{r}) = \sum_a C_{ad} \chi_a^i(\mathbf{r}), \quad (\text{A1})$$

$$\phi_l(\mathbf{r}) = \sum_b C_{bl} \chi_b^f(\mathbf{r}), \quad (\text{A2})$$

where

$$\chi_a(\mathbf{r}) = (r_1 - r_{1a})^{n_{1a}} (r_2 - r_{2a})^{n_{2a}} (r_3 - r_{3a})^{n_{3a}} \times \sum_{\alpha} B_{a\alpha} \exp(-S_{a\alpha} |\mathbf{r} - \mathbf{r}_a|^2).$$

Here, $B_{a\alpha}$ is a normalization coefficient, r_1 , r_2 , and r_3 are the Cartesian coordinates of \mathbf{r} , and the basis function is centered at \mathbf{r}_a .

The polarization matrix element in the direction ν is

$$\langle d | p_{\nu} | l \rangle = -i\hbar \int d^3r \phi_d^*(\mathbf{r}) \frac{\partial}{\partial r_{\nu}} \phi_l(\mathbf{r}) \quad (\text{A3})$$

$$= -i\hbar \sum_{ab} C_{ad} C_{bl} \Delta_{ab}^{\nu}, \quad (\text{A4})$$

where Δ^{ν} is the dipole matrix between basis elements

$$\Delta_{ab}^{\nu} = \int d^3r \chi_a^{i*}(\mathbf{r}) \frac{\partial}{\partial r_{\nu}} \chi_b^f(\mathbf{r}). \quad (\text{A5})$$

Standard procedures are available for calculating integrals of this type.²¹ The computation of Δ^{ν} is incorporated in quantum chemistry packages.

APPENDIX B: THE MANY-ELECTRON OVERLAPS

Determining the overlap factors $\langle \Phi_i^N c_l | \Phi_f'^{N+1} \rangle$ requires the $N+1$ electron valence wave functions $|\Phi_f'^{N+1}\rangle$ and $|c_l^{\dagger} \Phi_i^N\rangle$. This is routine for the ground state and low lying valence excitations using quantum chemistry codes. Rather than explicitly calculating deep-core excited states to determine the energies and dipole matrix elements, we assume that it is sufficiently localized to act as a point charge, and include its effect by replacing the nucleus of charge $+Z$ with a nucleus of charge $+Z+1$. This $Z+1$ approximation allows us to focus solely on the valence excitations.

The TDDFT or CI many-electron states are superpositions of Slater determinants

$$|c_l^{\dagger} \Phi_i^N\rangle = \sum_a J_{ai} |S_a\rangle, \quad (\text{B1})$$

$$|\Phi_f'^{N+1}\rangle = \sum_b J_{bf} |S_b\rangle, \quad (\text{B2})$$

where J are expansion coefficients and $|S_a\rangle$ is a (possibly excited) $N+1$ electron Slater determinant

$$|S_j\rangle = [(N+1)!]^{-1/2} \sum_{n=1}^{(N+1)!} (-1)^{P_n} P_n \{ |\phi_1\rangle \cdots |\phi_{N+1}\rangle \}, \quad (\text{B3})$$

$j = a, b.$

Here, P_n is one of the $(N+1)!$ possible permutations of the $N+1$ occupied orbitals. The factor $(-1)^{P_n}$ is 1 (-1) if an even (odd) number of interchanges of the orbitals has been made.

The overlap involves states calculated with a different set of orbitals, since the final state orbitals are computed in the field of the core hole, and, in the case of TDDFT expressed as a single Slater determinant, in the field of the

electron–valence hole excitation. The overlap of two Slater determinants with different sets of $N+1$ occupied orbitals is given by

$$\langle S_a | S_b \rangle = [(N+1)!]^{-1} \times \sum_{n,m} (-1)^{P_n+P'_m} \{ \langle \phi_{p_1} | \phi'_{p'_1} \rangle \cdots \langle \phi_{p_{N+1}} | \phi'_{p'_{N+1}} \rangle \} \quad (\text{B4})$$

$$= [(N+1)!]^{-1} \sum_{n,m} (-1)^{P_n+P'_m} T_{p_1 p'_1}^{ab} \cdots T_{p_{N+1} p'_{N+1}}^{ab} \quad (\text{B5})$$

$$= \sum_m (-1)^{P_m} T_{1 p'_1}^{ab} \cdots T_{N+1 p'_{N+1}}^{ab} \quad (\text{B6})$$

$$= \text{Det } T^{ab}, \quad (\text{B7})$$

where $T_{ij}^{ab} = \langle \phi_i | \phi'_j \rangle$ are the individual orbital overlaps and in the third step we have reordered the $(N+1)!$ terms in the sum. Note that T_{ij}^{ab} only contains overlaps between occupied orbitals. The difference in the matrices T^{ab} for different excitations a and b come from the inclusion of different sets of occupied orbitals.

Combining Eqs. (B1), (B2), and (B7) we finally obtain for the overlaps of the many-body states

$$\langle \Phi_i^N | c_l | \Phi_f^{N+1} \rangle = \sum_{ab} J_{ai} J_{bf} \text{Det } T^{ab}. \quad (\text{B8})$$

To calculate the orbital overlap matrix T , we expand the orbitals in a Gaussian basis set as described in Appendix A to find

$$T_{ij} = \langle \phi_i | \phi'_j \rangle \quad (\text{B9})$$

$$= \int d^3 r \phi_i^*(\mathbf{r}) \phi'_j(\mathbf{r}) \quad (\text{B10})$$

$$= \sum_{cd} C_{ci} C_{dj} \kappa_{cd}, \quad (\text{B11})$$

where κ is the overlap matrix between basis elements

$$\kappa_{cd} = \int d^3 r \chi_c^{i*}(\mathbf{r}) \chi_d^f(\mathbf{r}). \quad (\text{B12})$$

The elements of κ are part of the standard output of many quantum chemistry programs and their detailed calculations have been described elsewhere.²¹

APPENDIX C: RELATIVISTIC CORE-HOLE ENERGIES

A quantum chemistry calculation provides the total energy of the molecule. However, in the $Z+1$ approximation, it gives the energy for a molecule with the absorbing atom replaced by an atom with a more highly charged nucleus, not the desired energy of the molecule with a core hole. Further, quantum chemistry programs typically neglect relativistic effects that are important for core excitation energies. On the other hand, relativistic atom codes can give good estimates for the core excitation energies of atoms, but not of molecules.

To estimate the initial and final state energies, we separate the energy of the system into a component coming from the core electrons of the absorbing atom Ω , the energy of the valence electrons E^v , and the energy of the remaining atomic cores Ξ . If the core contains a hole, we label the core energy with an asterisk Ω^* . Thus $E_i = E_i^v + \Omega + \Xi$, $E_f = E_f^v + \Omega^* + \Xi$, and $E_i - E_f = E_i^v - E_f^v + \Omega - \Omega^*$. A quantum chemistry code can provide an accurate energy for the valence electrons E^v and a relativistic atom code gives an accurate energy for the ground state E_{at} and lowest energy core excited state E_{at}^* atoms. The poorly estimated core energy from the quantum chemistry code will be denoted Ω_{qc}^Z for the core filled atom and Ω_{qc}^{Z+1} for the $Z+1$ atom. The total energy from the quantum chemistry code will be denoted by the superscript qc , thus E^{qc} . We can now write $E_i^{qc} = E_i^v + \Omega_{qc}^Z + \Xi_{qc}$, $E_f^{qc} = E_f^v + \Omega_{qc}^{Z+1} + \Xi_{qc}$, $E_{\text{at}} = E_{\text{at}}^v + \Omega$, $E_{\text{at}}^* = E_{\text{at}}^{*v} + \Omega^*$, $E_{\text{at}}^{qc} = E_{\text{at}}^v + \Omega_{qc}^Z$, and $E_{\text{at}}^{*,qc} = E_{\text{at}}^{*v} + \Omega_{qc}^{Z+1}$.

It is now easy to verify that

$$E_i = E_i^{qc} + E_{\text{at}} - E_{\text{at}}^{qc} - \Xi_{qc} + \Xi, \quad (\text{C1})$$

$$E_f = E_f^{qc} + E_{\text{at}}^* - E_{\text{at}}^{*,qc} - \Xi_{qc} + \Xi, \quad (\text{C2})$$

which gives for the resonant energy

$$E_i - E_f = E_i^{qc} - E_f^{qc} + E_{\text{at}} - E_{\text{at}}^* - E_{\text{at}}^{qc} + E_{\text{at}}^{*,qc}. \quad (\text{C3})$$

All quantities in Eq. (C3) can be computed with standard software packages.

¹R. W. Schoenlein, S. Chattopadhyay, H. H. W. Chong, T. E. Glover, P. A. Heimann, C. V. Shank, A. A. Zholents, and M. S. Zolotarev, *Science* **287**, 2237 (2000).

²C. Bressler and M. Chergui, *Chem. Rev. (Washington, D.C.)* **104**, 1781 (2004).

³A. L. Ankudinov, B. Ravel, J. J. Rehr, and S. D. Conradson, *Phys. Rev. B* **58**, 7565 (1998).

⁴L. Triguero, L. G. M. Pettersson, and H. Ågren, *Phys. Rev. B* **58**, 8097 (1998).

⁵M. Saes, C. Bressler, R. Abela, D. Grolimund, S. L. Johnson, P. A. Heimann, and M. Chergui, *Phys. Rev. Lett.* **90**, 047403 (2003).

⁶P. Nozieres and C. T. DeDominicis, *Phys. Rev.* **178**, 1097 (1969).

⁷D. C. Langreth, *Phys. Rev. B* **1**, 471 (1970).

⁸G. D. Mahan, *Many-Particle Physics* (Plenum, New York, 1990).

⁹R. Zeller, *Z. Phys. B: Condens. Matter* **72**, 79 (1988).

¹⁰A. Vlček, Jr., *Coord. Chem. Rev.* **200–202**, 933 (2000).

¹¹H. Yersin, W. Humbs, and J. Strasser, *Coord. Chem. Rev.* **159**, 325 (1997).

¹²N. H. Damrauer, G. Cerullo, A. Yeh, T. R. Boussie, C. V. Shank, and J. K. McCusker, *Science* **275**, 54 (1997).

¹³A. D. Becke, *J. Chem. Phys.* **98**, 5648 (1993).

¹⁴C. Lee, W. Yang, and R. G. Parr, *Phys. Rev. B* **37**, 785 (1988).

¹⁵A. R. Dunn, I. J. Dmochowski, A. M. Bilwes, H. B. Gray, and B. R. Crane, *Proc. Natl. Acad. Sci. U.S.A.* **98**, 12420 (2001).

¹⁶D. P. Rillema, D. S. Jones, C. Woods, and H. A. Levy, *Inorg. Chem.* **31**, 2935 (1992).

¹⁷M. Biner, H. B. Buerger, A. Ludi, and C. Roehr, *J. Am. Chem. Soc.* **114**, 5197 (1992).

¹⁸A. L. Ankudinov, S. I. Zabinsky, and J. J. Rehr, *Comput. Phys. Commun.* **98**, 359 (1996).

¹⁹L. Hedin, *Phys. Rev.* **139**, A796 (1965).

²⁰S. Mukamel, *Principles of Nonlinear Optical Spectroscopy* (Oxford University Press, New York, 1995).

²¹D. B. Cook, *Handbook of Computational Quantum Chemistry* (Oxford University Press, New York, 1998).